SPATIO-TEMPORAL ANALYSIS OF THE STRUCTURES IN HIGH-PRESSURE TRANSCRITICAL FLUID FLOWS

G. BAREA[1] AND L. JOFRE[1]

[1] Department of Fluid Mechanics
Universitat Politècnica de Catalunya · BarcelonaTech (UPC), Barcelona 08019, Spain
e-mails: guillem.barea@upc.edu, lluis.jofre@upc.edu

Key words: Model Order Reduction, Proper Orthogonal Decomposition, Supercritical Fluids

Summary. This study explores the principal modes of high-pressure transcritical channel flow from direct numerical simulation data. The four cases investigated correspond to CO_2 at high-pressure conditions ($P/P_c = 1.5$) confined between a cold/bottom wall ($T/T_c = 0.8 - 0.95$) and a hot/top wall ($T/T_c = 1.1 - 1.4$). The bulk velocity ranges between $U_b = 0.5 - 1.0\,\mathrm{m/s}$ with corresponding bulk Reynolds numbers of $Re_b \approx 1000 - 2500$. In laminar cases, energy is predominantly concentrated in the initial modes, with approximately 95% of the energy captured by the first mode. Conversely, turbulent cases exhibit a broader distribution of energy across multiple modes, necessitating 50 to 100 modes to encapsulate the system's key characteristics. This disparity underscores the multiscale phenomena inherent in turbulent flows. Furthermore, thermodynamic variables in turbulent regimes demonstrate slower energy decay, particularly in later modes, indicating complex flow structures. These findings emphasize the necessity for detailed thermodynamic modeling to accurately capture the flow dynamics in high-pressure transcritical environments.

1 INTRODUCTION

Over the past decades, numerous research works have significantly contributed to the understanding of fluids surpassing their critical point, referred to as supercritical fluids. These fluids naturally occur in environments like for example undersea flows when their thermodynamic states reach critical values. While these conditions can be artificially replicated, leading to various engineering applications in fields such as water-cooled reactors, gas turbines, and liquid rocket engines [1, 2]. Although the study of supercritical fluids continues to be of crucial importance due to their incomplete understanding. Moreover, recent studies have shown that operating at high-pressure transcritical conditions enables the achievement of sustained turbulence in microfluidic flows by leveraging the unique thermophysical properties of supercritical fluids [3, 4, 5, 6]. In this context, it is crucial to distinguish between supercritical gas-like and liquid-like fluids, which are separated by the pseudo-boiling line [7, 2]. Although these studies are recent and do not completely detail the causality of the turbulent phenomena observed, it is evident that the nature of supercritical fluids, which are characterized by drastic thermophysical changes when crossing the pseudo-boiling line, introduce destabilizing baroclinic-based instabilities that promote laminar-to-turbulent transition. These instabilities, capable of altering the multiscale topology of wall-bounded turbulence, have been observed for example by Barea et al. [8]. In this regard, extracting meaningful experimental data from such

high-pressure transcritical systems is extremely complex, and for some variables, it may even be impossible [9]. Moreover, computationally resolving all scales in this type of systems is challenging due to the non-linearity of turbulent flows combined with the substantial variations in thermodynamic quantities. Therefore, identifying the most critical phenomena of these flows is (i) essential for understanding the underlying principles governing them, and (ii) critical for developing reduced-order models in the future.

In recent years, with the increase in computational power, large-scale high-fidelity simulations have become essential for he comprehensive study, characterization and modeling of flow physics problems. However, when studying significantly complex flows, like for example high-Reynolds-number turbulence and/or high-pressure transcritical fluids, the complexity and computational cost of the simulations increase exponentially [10, 11], making it impractical to rely solely on high-fidelity models. Consequently, low-fidelity models are often employed to make the problem tractable within reasonable time/cost frames. The POD methodology was first introduced to the fluid mechanics community by Lumley et al. [12] to advance the understanding of coherent structures in turbulent flows. This method decomposes the original flow into a linear combination of spatially dependent modes and their corresponding time-dependent coefficients, facilitating in this manner the detailed analysis of complex flow patterns. Due to its versatility, POD has been applied to a wide range of flow phenomena, including incompressible [13], compressible [14], two-phase [15], and supersonic flows [16]. For instance, POD has been instrumental in identifying which eddies contain the highest degree of energy [17, 18], and in providing a deeper energetic understanding of lid-driven cavity flows [19, 20]. The popularity of the method has led to various adaptations tailored to specific problems. Taira et al. [21] reviewed these variations, highlighting methods like balanced POD (BPOD) for flow control problems and the snapshot POD method, which solves a smaller eigenvalue problem and is well-suited for large datasets. The versatility of POD approaches and relatively straightforward implementation have contributed to its widespread use. In particular, its ability to provide a set of orthogonal basis vectors that reduce the dimensionality of complex flows by filtering out the effects from high-order modes makes it particularly appealing for multiscale systems.

The aim of this work, therefore, is to thoroughly study and characterize the energy decay of high-pressure transcritical fluid system using the POD method for various channel flow configurations. These configurations are first categorized into two typical fluid flow regimes: (i) laminar-like, and (ii) turbulent-like, all maintained under high-pressure transcritical conditions. To that end, the paper is organized as follows. Section 2 provides a detailed description of the flow physics modeling utilized to study high-pressure transcritical fluids, including the equations of fluid motion, real-gas thermodynamics, high-pressure transport coefficients, and the numerical methods utilized. In Section 3 the specific POD methodology employed to reduce the dimensionality and characterize the complex flow physics is detailed. Next, Section 4 presents an exhaustive description of the computational setup, followed by a comprehensive overview and characterization of the different cases considered in the study, classifying them as either laminar-like or turbulent-like. Section 5, discusses the results of the eigenanalysis. Where a deep study about the energy decay of the eigenvalues of velocity, temperature and specific heat will be done, in order to, understand if the thermodynamic variables need a bigger data sample to converge over hydrodynamic quantities. Finally, conclusions and future directions are proposed in Section 6.

2 FLOW PHYSICS MODELLING

The framework utilized for studying supercritical fluids turbulence in terms of (i) equations of fluid motion, (ii) real-gas thermodynamics, (iii) high-pressure transport coefficients, and (iv) numerical method is described below.

2.1 Equations of Fluid Motion

The flow motion of high-pressure transcritical fluids is described by the conservation of mass, momentum, and total energy, which in dimensionless form are written as

$$\frac{\partial \rho^\star}{\partial t^\star} + \nabla^\star \cdot (\rho^\star \boldsymbol{u}^\star) = 0, \tag{1}$$

$$\frac{\partial (\rho^\star \boldsymbol{u}^\star)}{\partial t^\star} + \nabla^\star \cdot (\rho^\star \boldsymbol{u}^\star \boldsymbol{u}^\star) = -\nabla^\star P^\star + \frac{\nabla^\star \cdot \boldsymbol{\tau}^\star}{Re_b}, \tag{2}$$

$$\frac{\partial (\rho^\star E^\star)}{\partial t^\star} + \nabla^\star \cdot (\rho^\star \boldsymbol{u}^\star E^\star) = \frac{\nabla^\star \cdot (\kappa^\star \nabla^\star T^\star)}{Re_b Br_b} - \nabla^\star \cdot (P^\star \boldsymbol{u}^\star)$$
$$+ \frac{\nabla^\star \cdot (\boldsymbol{\tau}^\star \cdot \boldsymbol{u}^\star)}{Re_b}, \tag{3}$$

where superscript $\star$ denotes normalized quantities, t is the time, $\boldsymbol{u}$ is the velocity vector, ρ is the density, P is the pressure, $\boldsymbol{\tau} = \mu(\nabla \boldsymbol{u} + \nabla^\mathsf{T} \boldsymbol{u}) - (2\mu/3)(\nabla \cdot \boldsymbol{u})\boldsymbol{I}$ is the viscous stress tensor with μ the dynamic viscosity and $\boldsymbol{I}$ the identity matrix, $E = e + |\boldsymbol{u}|^2/2$ and e are the total and internal energy, respectively, T is the temperature, and κ is the thermal conductivity. The obtention of these dimensionless equations is fundamented on the following set of inertial-based scalings [22, 23]

$$\boldsymbol{x}^\star = \frac{\boldsymbol{x}}{D_h}, \quad \boldsymbol{u}^\star = \frac{\boldsymbol{u}}{U_b}, \quad \rho^\star = \frac{\rho}{\rho_b}, \quad T^\star = \frac{T}{T_b},$$
$$P^\star = \frac{P}{\rho_b U_b^2}, \quad E^\star = \frac{E}{U_b^2}, \quad \mu^\star = \frac{\mu}{\mu_b}, \quad \kappa^\star = \frac{\kappa}{\kappa_b}, \tag{4}$$

with subscript b indicating bulk quantities, $\boldsymbol{x}$ the position vector, D_h the hydraulic diameter, and U the time-averaged streamwise velocity. The resulting set of scaled equations includes two dimensionless numbers: (i) bulk Reynolds number $Re_b = \rho_b U_b D_h/\mu_b$ characterizing the ratio between inertial and viscous forces; and (ii) bulk Brinkman number $Br_b = \mu_b U_b^2/(\kappa_b T_b)$, where c_P is the isobaric heat capacity, relating heat produced by viscous dissipation and heat transported by molecular conduction. The Brinkman number can be also expressed as $Br_b = Pr_b Ec_b$ containing the bulk Prandtl number $Pr_b = \mu_b c_{Pb}/\kappa_b$, where c_P is the isobaric heat capacity, quantifying the ratio between momentum and thermal diffusivity, and the bulk Eckert number $Ec_b = U_b^2/(c_{Pb} T_b) \approx U_b^2/(c_{Pb} \Delta T)$ accounting for the ratio between advective mass transfer and heat dissipation potential.

2.2 Real-Gas Thermodynamics

The thermodynamic space of solutions for the state variables pressure P, temperature T, and density ρ of a monocomponent fluid is described by an equation of state. One popular choice for systems at high pressures is the Peng-Robinson [24] equation of state. In general form, it can

be expressed in terms of the compressibility factor Z, which in dimensionless form is written as

$$P^\star = \frac{Z\rho^\star T^\star}{\hat{\gamma}_b Ma_b^2},$$

(5)

where $\hat{\gamma} \approx Z(c_P/c_V)[(Z + T(\partial Z/\partial T)_\rho)/(Z + T(\partial Z/\partial T)_P)]$ is an approximated real-gas heat capacity ratio [25] with c_V the isochoric heat capacity. As it can be noted, the dimensionless bulk Mach number $Ma_b = U_b/c_b$ appears, where c_b is the bulk speed of sound, which represents the ratio of flow velocity to the local speed of sound. In addition, real-gas equations of state need to be supplemented with the corresponding high-pressure thermodynamic variables (e.g., internal energy, heat capacities) based on departure functions [26] calculated as a difference between two states. In particular, their usefulness is to transform thermodynamic variables from ideal-gas conditions (low pressure - only temperature dependant) to supercritical conditions (high pressure). The ideal-gas parts are calculated by means of the NASA 7-coefficient polynomial [27], while the analytical departure expressions to high pressures are derived from the Peng-Robinson equation of state as detailed, for example, in Jofre & Urzay [2].

2.3 High-Pressure Transport Coefficients

The high pressures involved in the analyses conducted in this work prevent the use of simple relations for the calculation of dynamic viscosity μ and thermal conductivity κ. In this regard, standard methods for computing these coefficients for Newtonian fluids are based on the correlation expressions proposed by Chung et al. [28, 29]. These correlation expressions are mainly function of critical temperature T_c and density ρ_c, molecular weight W, acentric factor ω, association factor κ_a and dipole moment $\mathcal{M}$, and the NASA 7-coefficient polynomial [27]; further details can be found in dedicated works, like for example Poling *et al.* [30] and Jofre and Urzay [2].

3 DATA-DRIVEN ANALYSIS FRAMEWORK

POD is a MOR technique capable of extracting the most dominant modes in a field variable. Conceived by Lumley [31] as a mathematical tool to extract coherent structures from turbulent flow fields, POD soon became a prominent method for studying turbulent flow phenomena. The basis of this method predates its specific application, being fundamentally a matrix diagonalization technique. Today, various names, such as principal component analysis (PCA) and empirical component analysis, are used for different applications, which are based on a similar approach. The procedure to obtain POD modes involves decomposing the field into a linear combination of space-dependent eigenvectors and time-dependent coefficients as follows

$$\mathbf{x}(t) = \mathbf{q}(\xi, t) - \bar{\mathbf{q}}(\xi) = \sum_j a_j(t)\phi(\xi),$$

(6)

where $\mathbf{q}(\xi, t)$ is the vector field of the chosen variable with its temporal mean $\bar{\mathbf{q}}(\xi)$, $\phi(\xi)$ corresponds to the spatially-orthogonal modes, and the temporal coefficients are represented as $a_j(t)$. For channel flow configurations, the temporal mean $\bar{\mathbf{q}}(\xi)$ is only dependant on the values in the wall-normal direction due to the symmetries in the streamwise and spanwise directions, similar to the process followed by Nikolaidis et al. [32]. Each j corresponds to a time instant, representing a specific snapshot of the database generated [33]. Finally, the solution to the proposed problem is found by determining the eigenvalues λ_j and eigenvectors ϕ_j of Eq. 6.

The purpose of the following method is to determine the minimum set of basis functions capable of describing a flow field $\mathbf{q}(\xi, t)$ with a selected accuracy. The way to obtain a solution to this problem is to find the eigenvalues λ_j and eigenvectors ϕ_j of an associated covariance matrix R, defined in Eq. 8, or through the use of a singular value decomposition (SVD) of the snapshot matrix X, presented in Eq. 9, in the form

$$R\phi_j = \lambda_j \phi_j, \tag{7}$$

$$R = \sum_{j=1}^{m} \mathbf{q}(\xi, t_j)\, \mathbf{q}^T(\xi, t_j) = XX^T \in \mathbb{R}^{n \times n}, \tag{8}$$

$$X = [\, \mathbf{q}(\xi, t_1) \quad \mathbf{q}(\xi, t_2) \quad \dots \quad \mathbf{q}(\xi, t_m)\,], \tag{9}$$

where subindexes m and n correspond, respectively, to the total number and size of the flow snapshots considered and number of degrees of freedom of the data. In detail, the snapshot matrix is constructed by gathering in columns the fluctuations of the desired variable as defined in Eq. 6. The eigenvectors of this snapshot matrix are the so-called POD modes, whose inner product, defined as an integral over the spatial domain Ω, satisfies the orthonormality condition $\langle \phi_j, \phi_k \rangle = \int_\Omega \phi_j \cdot \phi_k \, d\Omega$ such that $j, k = 1, \dots, n$.

Once the eigenvalues and eigenvectors are calculated, the next step is to determine the number of eigenvalues needed to "accurately" represent the entire flow field. A popular approach is to consider r first eigenvalues such that [21] $\sum_{j=1}^{r} \sigma_j / \sum_{j=1}^{n} \sigma_j \approx 1$, this process is known as truncation. After performing it correctly, a much smaller dimension of the original data is obtained, enabling the flow to be represented as a truncated series expressed as

$$\mathbf{q}(\xi, t) - \bar{\mathbf{q}}(\xi) = \sum_{j}^{r} a_j(t)\phi(\xi). \tag{10}$$

Finally, the temporal coefficients from the high-dimensional data are determined by

$$a_j(t) = \langle \mathbf{q}(\xi, t) - \bar{\mathbf{q}}(\xi), \phi_j(\xi) \rangle. \tag{11}$$

Moreover, the obtention of the eigenvalues and eigenvectors can be performed in several ways, such as using (i) the "Method of Snapshots", which is designed for problems where the data is too large to be handled by the usual method, and (ii) the "SVD method", which utilizes the snapshot matrix X decomposed as

$$X = \Phi\Sigma\Psi^T, \tag{12}$$

where Φ and Ψ correspond, respectively, to the left and right singular vectors, and Σ is a diagonal matrix containing the singular values of X. It is important to highlight that this method is only valid for rectangular matrices.

Particularly to this work, the intricate configuration of the flow system studied may pose challenges when solely examining velocity fluctuations. Therefore, the modal analysis will incorporate also temperature and specific isobaric heat capacity as additional variables to account for thermodynamic variations within the system. In addition, correlations between hydrodynamic (velocity) and thermodynamic (temperature and specific isobaric heat capacity) variables will be analyzed with the aim to discern whether the corresponding modes are interconnected.
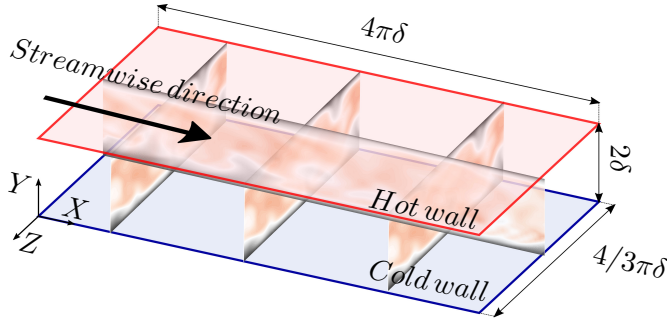
Figure 1: Channel flow schematics.

4 PROBLEM SETUP & DATABASE

This section delves into two pivotal aspects of the study: (i) description of the computational configuration, and (ii) characterization of flow regimes. The first part entails an intricate examination of the computational setup across the four distinct cases considered, highlighting both the common and differing aspects of each case. Subsequently, the second part presents an analysis of the first- and second-order flow statistics for each case.

4.1 Computational Configuration

The four cases studied in this work are part of an open-access dataset [33], which features different high-pressure transcritical channel flows as schematically represented in Fig. 1. In particular, the fluid selected is CO_2, whose critical pressure and temperature are $P_c = 7.4\,\text{MPa}$ and $T_c = 304.1\,\text{K}$, respectively. The fluid system operates at a supercritical bulk pressure of $P_b/P_c = 1.5$ and is confined between cold (cw) and hot (hw) isothermal walls, separated by a distance of $H = 2\delta$ with $\delta = 100\,\mu\text{m}$ representing the channel half-height. The temperature ranges from $T_{cw}/T_c = 0.8 - 0.95$ on the cold wall to $T_{hw}/T_c = 1.1 - 1.4$ on the hot wall, as detailed in Table 1. This setup causes the fluid to undergo a transcritical trajectory, operating within a thermodynamic region across the pseudo-boiling line [3, 8]. Finally, the flow moves from left to right in the streamwise direction, with a bulk velocity ranging between $U_b = 0.5$ and $1\,\text{m/s}$.

The computational domain is $4\pi\delta \times 2\delta \times (4/3)\pi\delta$ in the streamwise (x), wall-normal (y), and spanwise (z) directions, respectively. The streamwise and spanwise boundaries are set periodic, and no-slip conditions are imposed on the horizontal boundaries (x-z planes). The grid is uniform in the streamwise and spanwise directions with resolutions in wall units (based on cw values) equal to $\Delta x^+ \approx 0.5$ and $\Delta z^+ \approx 0.15$, and stretched toward the walls in the vertical direction with the first grid point at $y^+ = yu_{\tau,cw}/\nu_{cw} \approx 0.1$ and with sizes in the range $0.15 \lesssim \Delta y^+ \lesssim 1.65$. Thus, based on preliminary studies, this grid arrangement corresponds to a DNS of size $96 \times 96 \times 96$ grid points. The simulation strategy starts from a linear velocity profile with random fluctuations [34], which is advanced in time to reach turbulent steady-state conditions after approximately 5 flow-through-time (FTT) units; based on the bulk velocity U_b and the length of the channel $L_x = 4\pi\delta$, a FTT is defined as $t_b = L_x/U_b \sim \delta/u_\tau$. Finally, flow statistics are collected for roughly 10 FTTs once steady-state conditions are achieved.

The series of cases analyzed in this study is detailed in table 1, denoted by letters A, B, C, and

	P_b/P_c	T_{cw}/T_c	T_{hw}/T_c	U_b [m/s]	Re_b	Pr_b	Ec_b	Br_b	Ma_b
A	1.5	0.95	1.1	0.5	1050	2.7	2.0e-7	5.7e-7	3.0e-2
B	1.5	0.95	1.1	1.0	2363	2.8	8.0e-7	2.3e-6	1.6e-2
C	1.5	0.9	1.2	1.0	2109	2.3	1.0e-6	2.3e-6	7.3e-2
D	1.5	0.8	1.4	1.0	2022	2.4	1.0e-6	2.5e-6	6.6e-2

Table 1: Case setup and its dimensionless parameters.

D. While all cases maintain the same pressure ratio, they differ in their temperature differentials between walls, denoted as $\Delta T = [0.15, 0.15, 0.3, 0.6]$ for each respective case. Notably, the Reynolds bulk number is largely contingent on the mean velocity, as exemplified in case A where the velocity is 0.5, resulting in $Re_b \approx 1000$, while other cases range from $Re_b \approx 2000 - 2350$. Additionally, the bulk Prandtl number across all cases indicates that heat transfer is predominantly influenced by fluid viscosity rather than system dynamics. The significance of thermodynamic variables, particularly temperature and specific heat, is underscored by Eckert number analysis, which highlights the dominance of enthalpy change in the boundary layer over kinetic energy. The Brinkman number further elucidates that heat variation primarily stems from differentially-heated walls. Despite variations in density, the low velocities characteristic of these cases classify them as low-Mach, where shock waves are absent but thermodynamic fluctuations persist.

5 ENERGY DECAY

Figure 2 shows the decay of energy accumulated in the eigenvalues of the most energetic modes of velocity (a), temperature (b), and specific isobaric heat capacity (c). In detail, through an SVD procedure, eigenvalues are systematically arranged according to their respective energetic magnitudes. The initial modes are characterized by higher energy content, gradually diminishing in significance as one progresses towards the last modes, which exhibit substantially reduced energy levels spanning multiple orders of magnitude. In this regard, a general overview of the plot shows that cases A/C decay several orders of magnitude faster than cases B/D. The former group corresponds to the laminar cases, where most of the energy is allocated in the initial modes, as it can be seen in Table 2 where, for example, the energy contribution of the first mode is around 95%. However, this is not the case for the latter group, which corresponds to the turbulent flow cases characterized by an intrinsic multiscale nature that impacts significantly the energy decay of the modes. For the turbulent-like cases (B and D), the number of modes required to represent the main energetics of the flow is roughly between 50 and 100. Moreover, although the energy decay rate of velocity and thermodynamic modes for the turbulent cases is similar, there is a difference in slope between them above index (approximately) 200 where the latter decay at a slower rate.

In connection to the discussion above, Tables 2, 3 and 4 provide quantitative information of the energy spectrum distribution. Particularly, the tables present the cumulative contribution of the principal modes with respect to the first and more energetic ones, and the cumulative energy earn from one mode to the other. The first observation to highlight is how fast the energy of the first modes decreases for the laminar cases (A/C); viz. the fifth mode already gathers 97% of the total energy of the spectrum for both hydrodynamic and thermodynamic quantities.

	Case A	Case B	Case C	Case D
Mode	λ/λ_1 (%)	λ/λ_1 (%)	λ/λ_1 (%)	λ/λ_1 (%)
1	$1.0(38.7\%)$	$1.0(23.1\%)$	$1.0(96.5\%)$	$1.0(18.6\%)$
5	$1.4 \times 10^{-1}(97.1\%)$	$1.8 \times 10^{-1}(48.0\%)$	$1.2 \times 10^{-3}(97.1\%)$	$1.8 \times 10^{-1}(41.1\%)$
10	$7.0 \times 10^{-3}(99.7\%)$	$7.4 \times 10^{-2}(61.8\%)$	$5.9 \times 10^{-6}(99.7\%)$	$1.1 \times 10^{-1}(52.7\%)$
50	$8.0 \times 10^{-5}(99.9\%)$	$1.2 \times 10^{-2}(90.6\%)$	$1.0 \times 10^{-10}(99.9\%)$	$2.1 \times 10^{-2}(87.0\%)$
100	$4.5 \times 10^{-10}(99.9\%)$	$2.5 \times 10^{-3}(97.5\%)$	$2.2 \times 10^{-13}(99.9\%)$	$4.8 \times 10^{-3}(96.1\%)$
200	$7.5 \times 10^{-13}(99.9\%)$	$2.7 \times 10^{-4}(99.8\%)$	$6.8 \times 10^{-16}(99.9\%)$	$6.5 \times 10^{-3}(99.7\%)$

Table 2: Eigenvalue energy decay of the velocity variation in streamwise direction. Eigenvalues normalized by their maximum and energy contribution for each mode expressed as a percentage.

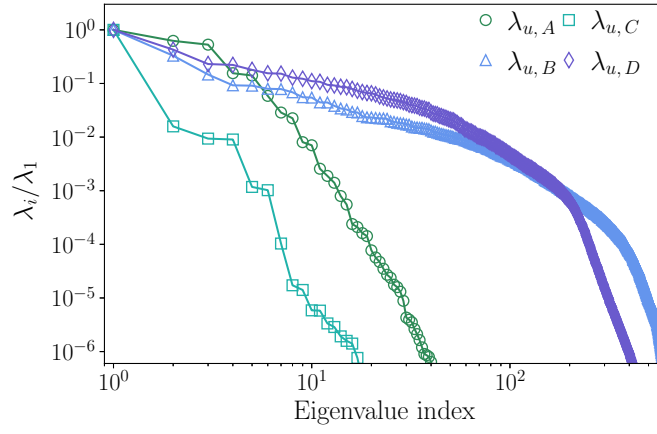|	Case A	Case B	Case C	Case D
Mode	λ/λ_1 (%)	λ/λ_1 (%)	λ/λ_1 (%)	λ/λ_1 (%)
1	$1.0(63.5\%)$	$1.0(21.7\%)$	$1.0(98.8\%)$	$1.0(8.0\%)$
5	$8.9 \times 10^{-2}(97.2\%)$	$8.9 \times 10^{-2}(38.6\%)$	$1.5 \times 10^{-4}(99.9\%)$	$3.2 \times 10^{-1}(24.2\%)$
10	$4.2 \times 10^{-3}(99.5\%)$	$5.5 \times 10^{-2}(45.3\%)$	$4.4 \times 10^{-6}(99.9\%)$	$2.1 \times 10^{-1}(33.5\%)$
50	$4.2 \times 10^{-6}(99.9\%)$	$1.6 \times 10^{-2}(66.4\%)$	$1.1 \times 10^{-9}(99.9\%)$	$6.8 \times 10^{-2}(68.1\%)$
100	$3.9 \times 10^{-8}(99.9\%)$	$8.4 \times 10^{-3}(78.4\%)$	$4.9 \times 10^{-12}(99.9\%)$	$2.8 \times 10^{-2}(85.1\%)$
200	$3.0 \times 10^{-11}(99.9\%)$	$3.8 \times 10^{-3}(90.5\%)$	$1.7 \times 10^{-14}(99.9\%)$	$7.5 \times 10^{-3}(97.9\%)$

Table 3: Eigenvalue energy decay of the temperature variation. Eigenvalues normalized by their maximum and energy contribution for each mode expressed as a percentage.

However, for the turbulent cases as it can be seen in Table 2, the energy contribution does not reach 90% until accumulating the first fifty velocity modes. Moreover, when observing the three variables at once for cases B/D, it is clear that they show a similar decay for the velocity eigenvalues (see Fig. 2; at least for the first 200 modes. However, as quantified in Tables 3 and 4, the thermodynamic variables exhibit a significantly slower energy decay in the first 50 modes. Notably, the specific isobaric heat capacity presents the slowest decay among the three variables. Specifically, as shown in Table 4 for cases B/D, only 90% of the energy is accumulated after collecting approximately 200 modes of the specific isobaric heat capacity. These results highlight several points: (i) increasing ΔT between walls makes the energy distribution between modes to be more spread (case D); (ii) maintaining the cold and hot wall temperatures closer to the pseudo-boiling temperature propitiates a slower energy decay at high eigenvalue indexes (case B), making it more challenging to gather the complete energy spectrum as depicted in Fig. 2; and (iii) initial modes of the thermodynamic variables contain important structures that are crucial for characterizing/modeling this type of problems as it is further discussed in the subsections below. In conclusion, to reduce the high dimensionality of such flow systems, while retaining meaningful information, modeling approaches should focus on considering the velocity modes but (especially) also the thermodynamic ones.

6 CONCLUSIONS

This study aimed to investigate the energy decay in four different wall-bounded high-pressure transcritical channel flow setups using eigenanlaysis via the SVD method. Initially, has been characterized the computational domain and briefly detailed the computational setup of each case. Subsequently, singular value decomposition (SVD) was performed to examine the energy
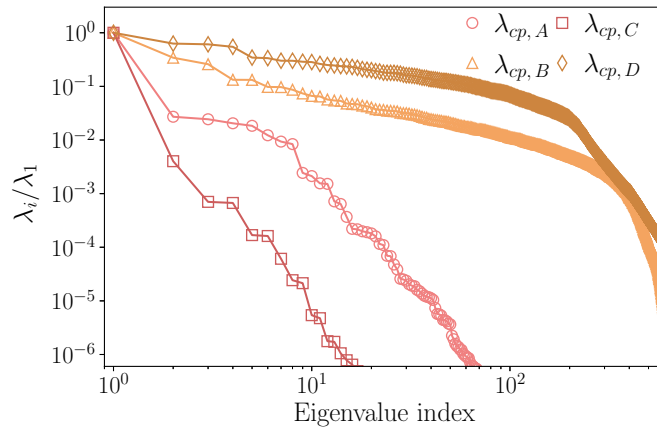
(a)
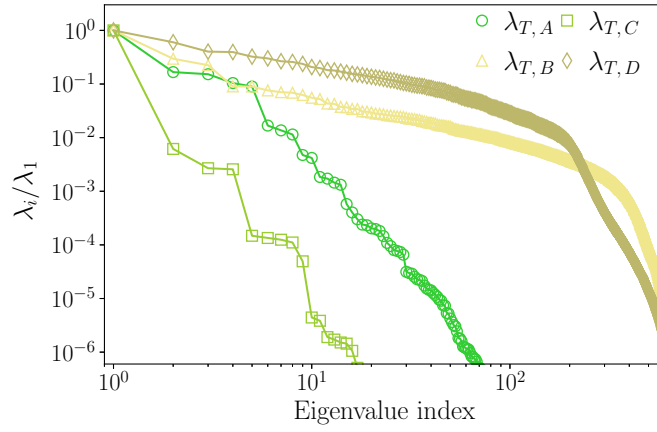
(b)

(c)

Figure 2: Eigenvalue decay for the velocity, temperature and specific heat vector field.

Mode	Case A λ/λ_1 (%)	Case B λ/λ_1 (%)	Case C λ/λ_1 (%)	Case D λ/λ_1 (%)
1	$1.0(88.3\%)$	$1.0(17.4\%)$	$1.0(99.4\%)$	$1.0(4.6\%)$
5	$1.8 \times 10^{-2}(97.4\%)$	$1.3 \times 10^{-1}(34.2\%)$	$1.6 \times 10^{-4}(99.9\%)$	$3.4 \times 10^{-1}(16.0\%)$
10	$2.1 \times 10^{-3}(99.5\%)$	$6.6 \times 10^{-2}(41.0\%)$	$5.4 \times 10^{-6}(99.9\%)$	$2.8 \times 10^{-1}(22.6\%)$
50	$3.6 \times 10^{-6}(99.9\%)$	$2.1 \times 10^{-2}(63.6\%)$	$8.8 \times 10^{-10}(99.9\%)$	$1.2 \times 10^{-1}(53.4\%)$
100	$3.3 \times 10^{-8}(99.9\%)$	$1.1 \times 10^{-2}(76.7\%)$	$7.2 \times 10^{-12}(99.9\%)$	$7.0 \times 10^{-2}(74.4\%)$
200	$4.6 \times 10^{-11}(99.9\%)$	$5.1 \times 10^{-3}(89.9\%)$	$2.8 \times 10^{-14}(99.9\%)$	$2.5 \times 10^{-3}(93.7\%)$

Table 4: Eigenvalue energy decay of the specific heat variation. Eigenvalues normalized by their maximum and energy contribution for each mode expressed as a percentage.

decay of the selected variables (u, T, c_P) by plotting and analyzing the eigenvalue decay for over 500 modes.

The results of this study revealed distinct energy decays for each variable. Firstly, two different groups can be discerned from the eigenanalysis: (i) the laminar-like cases, which decay rapidly as expected with just five modes; and (ii) the turbulent-like cases, which require between 50 to 200 modes to reach similar levels of accumulated energy, depending on whether they are hydrodynamic or thermodynamic variables. Secondly, it is notable that cases with a smaller ΔT, closer to the pseudo-boiling temperature, exhibit faster decay in both hydrodynamic and thermodynamic variables at the initial modes, indicating that the pseudo-boiling region might be easier to model.

Future research should focus on: (i) study the spatial and temporal structures to see if there are any coherent structures in high-pressure transcritical setups; (ii) determining whether the results observed are strictly related to spatial decomposition or if the main features exhibit frequency dependency; and (iii) developing a model capable of representing the pseudo-boiling region in low-fidelity simulations.

ACKNOWLEDGMENTS

References

[1] Jung Yul Yoo. The turbulent flows of supercritical fluids with heat transfer. *Annu. Rev. of Fluid Mech.*, 45:495–525, 1 2013.

[2] L. Jofre and J. Urzay. Transcritical diffuse-interface hydrodynamics of propellants in high-pressure combustors of chemical propulsion systems. *Prog. Energy Combust. Sci.*, 82:100877, 2021.

[3] M. Bernades, F. Capuano, and L. Jofre. Microconfined high-pressure transcritical fluids turbulence. *Phys. Fluids*, 35:015163, 2023.

[4] N. Masclans, F. Vázquez-Novoa, M. Bernades, R. M. Badia, and L. Jofre. Thermodynamics-informed neural network for recovering supercritical fluid thermophysical information from turbulent velocity data. *Int. J. Thermofluids*, 20:100448, 2023.

[5] C. Monteiro and L. Jofre. Flow regime analysis of high-pressure transcritical fluids in microducts. *Int. J. Heat Mass Trans.*, 224:125295, 2024.

[6] A. Abdellatif and L. Jofre. Empirical heat transfer correlations of high-pressure transcritical fluids at low Reynolds numbers. *Int. J. Heat Mass Transf.*, 231:125837, 2024.

[7] L. Jofre and J. Urzay. A characteristic length scale for density gradients in supercritical monocomponent flows near pseudoboiling. *Annual Research Briefs, Center for Turbulence Research, Stanford University*, pages 277–282, 2020.

[8] G. Barea, N. Masclans, and L. Jofre. Multiscale flow topologies in microconfined high-pressure transcritical fluid turbulence. *Phys. Rev. Fluids*, 8:054608, 2023.

[9] J. Westerweel, G. E. Elsinga, and R. J. Adrian. Particle image velocimetry for complex and turbulent flows. *Annu. Rev. of Fluid Mech.*, 45:391–421, 2013.

[10] T. R. Bewley, P. Moin, and R. Temam. DNS-based predictive control of turbulence: an optimal benchmark for feedback algorithms. *J. Fluid Mech.*, 447:179–225, 2001.

[11] J. Kim and A. Leonard. The early days and rise of turbulence simulation. *Annu. Rev. Fluid Mech.*, 56:21–44, 2023.

[12] J.L. Lumley. Coherent structures in turbulence. *Transition and Turbulence*, pages 215–242, 1981.

[13] G. Alfonsi and L. Primavera. The structure of turbulent boundary layers in the wall region of plane channel flow. *Proc. R. Soc. A: Math. Phys. Eng. Sci.*, 463(2078):593–612, 2007.

[14] C. W. Rowley, T. C., and R. M. Murray. Model reduction for compressible flows using POD and Galerkin projection. *Phys. D: Nonlinear Phenom.*, 189:115–129, 2004.

[15] D. Li, B. Zhao, and J. Wang. Data-driven identification of coherent structures in gas–solid system using proper orthogonal decomposition and dynamic mode decomposition. *Phys. Fluids*, 35:013321, 2023.

[16] J. Yu, C. Yan, and M. Guo. Non-intrusive reduced-order modeling for fluid problems: A brief review. *Proc. Inst. Mech. Eng. G: J. Aerosp. Eng.*, 233(16):5896–5912, 2019.

[17] P. Moin and Robert D Moser. Characteristic-eddy decomposition of turbulence in a channel. *J. Fluid Mech.*, 200:471–509, 1988.

[18] G. Berkooz, P. Holmes, and J. L. Lumley. The proper orthogonal decomposition in the analysis of turbulent flows. *Annu. Rev. Fluid Mech.*, 25(1):539–575, 1993.

[19] W. Cazemier, R. W. C. P. Verstappen, and A. E. P. Veldman. Proper orthogonal decomposition and low-dimensional models for driven cavity flows. *Phys. Fluids*, 10(7):1685–1699, 1998.

[20] D. Ahlman, F. Söderlund, J. Jackson, A. Kurdila, and W. Shyy. Proper orthogonal decomposition for time-dependent lid-driven cavity flows. *Numer. Heat Transf. B: Fundam.*, 42(4):285–306, 2002.

[21] K. Taira, S. L. Brunton, S. T. M. Dawson, C. W. Rowley, T. Colonius, B. J. McKeon, O. T. Schmidt, S. Gordeyev, V. Theofilis, and L. S. Ukeiley. Modal analysis of fluid flows: An overview. *AIAA J.*, 55(12):4013–4041, 2017.

[22] L. Jofre, Z. R. del Rosario, and G. Iaccarino. Data-driven dimensional analysis of heat transfer in irradiated particle-laden turbulent flow. *Int. J. Multiph. Flow*, 125:103198, 2020.

[23] L. Jofre, M. Bernades, and F. Capuano. Dimensionality reduction of non-buoyant microconfined high-pressure transcritical fluid turbulence. *Int. J. Heat Fluid Flow*, 102:109169, 2023.

[24] D. Y. Peng and D. B. Robinson. A new two-constant equation of state. *Ind. Eng. Chem. Fundam.*, 15:59–64, 1976.

[25] A. Firoozabadi. *Thermodynamics and Applications in Hydrocarbon Energy Production*. McGraw-Hill Education, New York (USA), 1st edition, 2016.

[26] W. C. Reynolds and P. Colonna. *Thermodynamics: Fundamentals and Engineering Applications*. Cambridge University Press, Cambridge (UK), 1st edition, 2019.

[27] A. Burcat and B. Ruscic. Third millennium ideal gas and condensed phase thermochemical database for combustion with updates from active thermochemical tables. Technical report, Argonne National Laboratory, 2005.

[28] T. H. Chung, L. L. Lee, and K. E. Starling. Applications of kinetic gas theories and multiparameter correlation for prediction of dilute gas viscosity and thermal conductivity. *Ind. Eng. Chem. Fund.*, 23:8–13, 1984.

[29] T. H. Chung, M. Ajlan, L. L. Lee, and K. E. Starling. Generalized multiparameter correlation for nonpolar and polar fluid transport properties. *Ind. Eng. Chem. Fund.*, 27:671–679, 1988.

[30] B. E. Poling, J. M. Prausnitz, and J. P. O'Connell. *Properties of gases and iquids*. McGraw Hill, New York (USA), 5th edition, 2001.

[31] *The Structure of Inhomogeneous Turbulent Flows*, 1967.

[32] M. A. Nikolaidis, P. J. Ioannou, B. F. Farrell, and A. Lozano-Durán. POD-based study of turbulent plane poiseuille flow: comparing structure and dynamics between quasi-linear simulations and DNS. *J. Fluid Mech.*, 962:A16, 2023.

[33] A. Abdellatif, C. Monteiro, M. Bernades, and L. Jofre. Microconfined high-pressure transcritical channel flow database: laminar, transitional & turbulent regimes. *Sci. Data*, 2024.

[34] K. S. Nelson and O. B. Fringer. Reducing spin-up time for simulations of turbulent channel flow. *Phys. Fluids*, 29:105101, 2017.